HHS Public Access

Author manuscript

Prog Neurobiol. Author manuscript; available in PMC 2022 August 01.

Published in final edited form as:

Prog Neurobiol. 2022 August ; 215: 102297. doi:10.1016/j.pneurobio.2022.102297.

Aberrant neural activity in prefrontal pyramidal neurons lacking TDP-43 precedes neuron loss

Bo Liang[a,1], **Rashmi Thapa**[b,1], **Gracie Zhang**[c], **Casey Moffitt**[d], **Yan Zhang**[d], **Lifeng Zhang**[d], **Amanda Johnston**[b], **Hyrum P. Ruby**[b], **Giovanni Barbera**[d], **Philip C. Wong**[e,g], **Zhaojie Zhang**[b], **Rong Chen**[f], **Da-Ting Lin**[d,g], **Yun Li**[b,*]

[a]School of Electrical Engineering & Computer Science, College of Engineering & Mines, University of North Dakota, 243 Centennial Drive Stop 7165, Grand Forks, ND 58202, USA

[b]Department of Zoology and Physiology, University of Wyoming, 1000 E University Avenue, Laramie, WY 82071, USA

[c]Laramie High School, 1710 Boulder Drive, Laramie, WY 82070, USA

[d]Intramural Research Program, National Institute on Drug Abuse, National Institutes of Health, 333 Cassell Drive, Baltimore, MD 21224, USA

[e]Department of Pathology, Johns Hopkins University School of Medicine, 725N. Wolfe Street, Baltimore, MD 21205, USA

[f]Department of Diagnostic Radiology and Nuclear Medicine, University of Maryland School of Medicine, 100N. Greene St., Baltimore, MD 21201, USA

[g]The Solomon H. Snyder Department of Neuroscience, Johns Hopkins University School of Medicine, 725N. Wolfe Street, Baltimore, MD 21205, USA

Abstract

Mislocalization of TAR DNA binding protein 43 kDa (TARDBP, or TDP-43) is a principal pathological hallmark identified in cases of neurodegenerative disorders such as amyotrophic lateral sclerosis (ALS) and frontotemporal dementia (FTD). As an RNA binding protein, TDP-43 serves in the nuclear compartment to repress non-conserved cryptic exons to ensure the normal transcriptome. Multiple lines of evidence from animal models and human studies support the view

*Corresponding author. yli30@uwyo.edu (Y. Li).

[1]These authors contributed equally.

Author's contributions

YL designed and supervised the studies. YL, LZ, YZ, and RT performed brain surgeries including viral injection and GRIN lens implantation. YL, CM, YZ, and RT performed repetitive in vivo calcium imaging. BL performed computational analysis of in vivo calcium imaging data. RC performed statistics including two-way repeated-measures ANOVA and forest plots. RT performed various immunostainings and Nissl staining. RT, GZ, and AJ collected confocal images and slide scanner images. RT and GZ performed data analysis for immunostaining and Nissl staining images. ZZ helped with confocal and slide scanner microscopy setup and data analysis for Nissl staining. CM, RT, and HR performed behavior annotation and verification. PW provided transgenic mouse line. BL, GB, and DTL constructed the miniscope recording system. YL, BL, and RT wrote the manuscript. DTL, ZZ, HR, and PW edited the manuscript. All authors read and approved the final manuscript.

Competing interests

The authors declare no competing interests.

Appendix A. Supporting information

Supplementary data associated with this article can be found in the online version at doi:10.1016/j.pneurobio.2022.102297.

that loss of TDP-43 leads to neuron loss, independent of its cytosolic aggregation. However, the underlying pathogenic pathways driven by the loss-of-function mechanism are still poorly defined. We employed a genetic approach to determine the impact of TDP-43 loss in pyramidal neurons of the prefrontal cortex (PFC). Using a custom-built miniscope imaging system, we performed repetitive in vivo calcium imaging from freely behaving mice for up to 7 months. By comparing calcium activity in PFC pyramidal neurons between TDP-43 depleted and TDP-43 intact mice, we demonstrated remarkably increased numbers of pyramidal neurons exhibiting hyperactive calcium activity after short-term TDP-43 depletion, followed by rapid activity declines prior to neuron loss. Our results suggest aberrant neural activity driven by loss of TDP-43 as the pathogenic pathway at early stage in ALS and FTD.

Keywords

Neurodegenerative disorders; In vivo calcium imaging; Aberrant neural activity; Hyperactivity; Hypoactivity

1. Introduction

TAR DNA-binding protein 43 kDa (TARDBP, or TDP-43) is a highly conserved nuclear DNA/RNA binding protein important for transcription regulation (Polymenidou et al., 2011; Tollervey et al., 2011). Mislocalization of TDP-43, either abnormally accumulated into cytosolic or nuclear inclusions, is a common pathological feature of several neurodegenerative diseases, including amyotrophic lateral sclerosis (ALS), frontotemporal dementia (FTD), and Alzheimer's disease (AD) (Amador-Ortiz et al., 2007; Janssens and Van Broeckhoven, 2013; Neumann et al., 2006). FTD and ALS sharing clinical, genetic, and pathological signatures, have been proposed to represent two extremes of one broad spectrum of neurodegenerative disorder (Ling et al., 2013). Missense mutations in TDP-43 have been identified in familial and sporadic ALS cases (Kabashi et al., 2008; Sreedharan et al., 2008), as well as, in rare FTD cases (Borroni et al., 2009; Kovacs et al., 2009). Most of these mutations are at the C-terminal region of TDP-43, which is important for interaction with members of heterogeneous nuclear ribonucleoproteins (hnRNPs) (Buratti et al., 2005). Association of TDP-43 genetic mutations with ALS and FTD supports the idea that TDP-43 is mechanistically linked to neurodegeneration. A gain-of-function mechanism due to TDP-43 cytoplasmic aggregates has been proposed to contribute to neurodegeneration (Lee et al., 2011; Ritson et al., 2010). In addition, a loss-of-function mechanism caused by TDP-43 nuclear clearance has also been implicated in the pathogenesis process (Vanden Broeck et al., 2014).

Several lines of evidence strongly support the loss-of-function mechanism as the major pathogenesis pathway towards neurodegeneration. First, studies from numerous TDP-43 knockdown and knockout models in worms, flies, fish and rodents (Chiang et al., 2010; Donde et al., 2019; Feiguin et al., 2009; Iguchi et al., 2013; Kraemer et al., 2010; Schmid et al., 2013; Zhang et al., 2012), indicate that decrease or loss of TDP-43 expression leads to neuron loss (Diaper et al., 2013; Donde et al., 2019; Iguchi et al., 2013; Vanden Broeck et al., 2013). Second, no correlation has been established between the presence

of cytoplasmic aggregates and neurodegeneration in transgenic mice expressing mutant forms of human TDP-43, where neurodegeneration occurs in motor neurons (Stallings et al., 2010; Wegorzewska et al., 2009; Wils et al., 2010), as well as pyramidal neurons in the frontal cortex of several mouse lines (Wegorzewska et al., 2009; Wils et al., 2010). These observations indicate that cytoplasmic aggregates are not required to induce neurodegeneration (Igaz et al., 2011; Wegorzewska et al., 2009). Third, clinical studies discover TDP-43 nuclear depletion occurs in brain neurons at a pre-symptomatic stage without cytoplasmic inclusions in some FTD cases (Nana et al., 2019; Vatsavayai et al., 2016), supporting the notion that loss of TDP-43 represents an early event that drives neuron loss. Fourth, TDP-43 serves in the nuclear compartment to repress nonconserved cryptic exons during RNA splicing (Ling et al., 2015), and incorporation of nonconserved cryptic exons has been documented not only in brain transcriptomes of ALS and FTD cases (Ling et al., 2015), but also in AD cases exhibiting TDP-43 pathology (Sun et al., 2017). Fifth, ALS-linked TDP-43 mutants from fibroblast-derived human motor neurons fail to repress nonconserved cryptic exons, independent of TDP-43 cytoplasmic aggregates (Klim et al., 2019; Melamed et al., 2019). Finally, TDP-43 also represses a cryptic exon splicing in *UNC13A*, a top genetic allele to increase risk for ALS and FTD (Brown et al., 2021; Ma et al., 2021).

All these observations highlight the need to understand the pathogenic mechanism by which TDP-43 loss-of-function drives neurodegeneration independent of its toxic gain-of-function from cytosolic inclusions. As a nuclear DNA/RNA binding protein, TDP-43 binds to UG-rich regions to regulate RNA processing, including mRNA splicing (Ling et al., 2015; Polymenidou et al., 2011; Tollervey et al., 2011). Although genome-wide analyses have identified a large number of genes and transcripts regulated by TDP-43 (Polymenidou et al., 2011; Tollervey et al., 2011), the disease-relevant pathways are still poorly defined. Emerging evidence suggests that neurodegeneration is related to progressive changes in individual neural activity and brain microcircuits. Aberrant neural activity and dysregulated calcium signaling have been documented in some mouse models of neurodegenerative diseases (Anekonda and Quinn, 2011; Busche et al., 2008; Lopez et al., 2008; Palop et al., 2007; Styr and Slutsky, 2018; Zhang et al., 2016). It is not clear whether TDP-43 loss-of-function mechanism drives aberrant neural activity prior to neuron loss.

We employed a genetic approach to determine the impact of TDP-43 loss on neural activity of pyramidal neurons from a mouse model. Several conditional TDP-43 knockout mouse lines have been developed to bypass embryonic lethality (Chiang et al., 2010; Iguchi et al., 2013; Kraemer et al., 2010), since TDP-43 is essential for early embryogenesis (Sephton et al., 2010; Wu et al., 2010). Among them, *Tdp-43*$^{F/F}$ mice is a mouse line in which the exon 3 of the mouse *Tdp-43* gene is flanked with two loxP sites (Chiang et al., 2010). In the presence of Cre recombinase, the TDP-43 coding sequence is disrupted and a stop codon is introduced prematurely. It was predicted that the truncated N-terminal TDP-43 fragment is nonfunctional, since it lacked the critical RNA-binding domain encoded by the exon 3 and the highly conserved C-terminal domain. It was later confirmed that even the predicted N-terminal TDP-43 fragment was not expressed upon Cre recombination (Chiang et al., 2010). To explore whether TDP-43 loss-of-function mediated neurodegeneration is related to aberrant calcium signaling in the cortical network, we measured calcium

activity in pyramidal neurons of the prefrontal cortex from awake behaving *Tdp-43*$^{F/F}$ mice, and compared calcium activity between TDP-43 depleted and control mice. We found that TDP-43 deletion induced aberrant neuronal activity changes, initially hyperactivity followed by a rapid activity decline, prior to neuron loss. These data implicate early dysfunctions in intracellular calcium signaling as a convergent point that may ultimately lead to neurodegeneration.

2. Methods

2.1. Animals

All experimental procedures were approved by the Institutional Animal Care and Use Committee of the University of Wyoming and the National Institute on Drug Abuse (NIDA), and were conducted in accordance with the guidelines of the National Institutes of Health. *Tardbp flox/flox* (loxP sites flank exon 3 of *Tardbp*) male and female breeders were obtained from Dr. Philip Wong's laboratory at the Johns Hopkins University School of Medicine. This mouse line was bred and maintained at the NIDA and the University of Wyoming. Mice were housed up to five mice per cage under a 12 h light/dark cycle and given ad libitum access to food and water.

2.2. Stereotaxic injection

18 male *Tardbp flox/flox* homozygous mice (*Tdp-43*$^{F/F}$) aged 3–5 months weighing 25–35 g were used for experiments, including 8 control mice and 10 knockout (KO) mice. Stereotaxic viral injection was performed bilaterally at the prelimbic region based on the published lab protocols (Thapa et al., 2021; Zhang et al., 2019). Mice were briefly anesthetized with 5 % isoflurane in oxygen. The head was shaved and held on a stereotaxic stage with a heating pad at 35 °C. Anesthesia was maintained with 1.5 % isoflurane in oxygen throughout the surgery. An incision was made along the sagittal midline to expose the bregma and lambda. A 0.6 mm dental burr was used to drill a small hole through the skull at the coordinates A/P: + 1.94 mm and M/L: 0.5 mm on both hemispheres. For KO mice, bilateral injection of a viral mixture was performed, containing AAV1-CaMKII-Cre (1.2×10^{13} GC/mL) and a Cre dependent AAV1-CAG-FLEX-GCaMP6f (1.3×10^{13} GC/mL) in a ratio of 1:1. For control mice, AAV1-CaMKII-GCaMP6f (2.8×10^{13} GC/mL) was diluted with saline in a ratio of 1:1. Through a microliter syringe controlled by a micro-pump, 500 nL of virus was infused into each side of the designated brain region (A/P: +1.94 mm, M/L: 0.5 mm, D/V: 1.75 mm) at a rate of 50 nL/minute. The virus was allowed to diffuse away for additional 5–10 min before the skull skin was stitched for closure. Mice were allowed to recover for 14 days before proceeding to the next step.

2.3. Gradient-index (GRIN) lens implantation

GRIN lens implantation into the mouse dorsal prelimbic cortex was performed according to the previously described lab protocols (Thapa et al., 2021; Zhang et al., 2019). Mice were anesthetized with an intraperitoneal injection of Ketamine/Xylazine (Ketamine: 100 mg/kg; Xylazine: 15 mg/kg) initially and maintained with additional doses of Ketamine (50 mg/kg) during the surgery. Craniotomy was performed at the coordinates A/P 1.94 mm and M/L 0.8 mm on the right side using a 1.2 mm drill burr. The brain tissue was aspirated layer-by-layer

to the depth of 1.8 mm (measured from the bregma), with a blunt-end 27-G needle that was connected to an in-house vacuum system. The needle holder was connected to a robotic arm inclined to a 10° angle laterally, and was controlled by a custom-built software (https://github.com/liang-bo/AutoStereota) (Liang et al., 2019). During the entire aspiration process, the exposed brain tissue was continuously rinsed with the artificial cerebrospinal fluid (ACSF) containing 124 mM of NaCl, 2.5 mM of KCl, 1.25 mM of NaH_2PO_4, 1.2 mM of $MgCl_2$, 25 mM of glucose, 26 mM of $NaHCO_3$ and 2.4 mM of $CaCl_2$. ACSF was bubbled with a gas mixture of 95 % O_2 and 5 % CO_2 and filtered through a 0.2 μm filter. After the aspirated area was blood-free, a sterile GRIN lens (GRINTECH) was implanted into the well and secured with two layers of dental cement (first layer-Metabond, second layer-Duralay). The exposed GRIN lens was covered by a customized protection cap.

2.4. Miniscope base mounting

All miniscopes used for the experiment were custom-built by Dr. Da-Ting Lin's group at NIDA IRP (Barbera et al., 2016; Liang et al., 2018; Zhang et al., 2021). After 4 weeks of GRIN lens implantation, a miniscope base was permanently mounted on the mouse skull. For base mounting, a miniscope fitted with a base was brought closer to the GRIN lens with the help of a custom-built motorized controller to obtain the best focal plane and the base was then affixed to the skull using dental cement. The main body of the miniscope was detached from the base after the dental cement had hardened.

2.5. In vivo calcium imaging during social behavior tests

Mice were briefly anesthetized with 5 % isoflurane in oxygen and the miniscope was fastened onto the base. Mice were allowed to recover from isoflurane for at least 30 min in their home cages before performing the in vivo recordings.

Social behavior test was performed based on the previously published protocol (Liang et al., 2018). The experiment was performed in an open square arena (42 cm × 42 cm × 30 cm) to facilitate calcium imaging where two small containers were placed near the two opposite corners (10 cm away from the sidewall of arena). The test was composed of two stages, "habituation (H)' and "sociability (SB)", each 10-minute long. During H stage, the mouse was allowed to explore the two empty containers freely. In SB stage, an age and gender matched (male) stranger mouse (stranger 1) was placed inside one of the containers whereas the other container remained empty. SB stage measures the tendency of a subject mouse to spend more time exploring the container holding a social target compared to the empty container.

For recording, the mouse was brought closer to the behavior arena and the miniscope was connected to a cable linked with the data acquisition computer system. Simultaneous recordings of the calcium imaging and mouse behavior were collected in two different computers with the aid of a custom-built calcium image recording software (Neu-View) and a behavior recording software (FlyCap2, FLIR). The behavior recording was triggered by NeuView so that both calcium and behavioral recordings were temporally synchronized frame by frame. The recordings were performed at a rate of 10 frames per second. Each 10-minute stage was broken down into two 5-minute recording sessions to prevent excessive

heating of the miniscope. Repetitive in vivo calcium imaging was performed every 4–6 weeks for longitudinal study until no active neurons were identified through in vivo calcium imaging. The investigators who collected in vivo calcium imaging data were blind regarding CTRL and KO groups.

For behavior analysis, the mouse behavior was manually annotated frame by frame using a MATLAB annotation program (https://github.com/pdollar/toolbox) and the time spent by the subject mouse exploring the containers was calculated. It was considered that the subject mouse was exploring when it sniffed, bit, poked, or physically contacted the container.

2.6. Calcium imaging data analysis

Calcium image processing: Calcium images were first registered using motion correction toolbox NoRMCorre (Pnevmatikakis and Giovannucci, 2017). Then a constrained non-negative matrix factorization (CNMF) based calcium image processing toolbox, CaImAn-MATLAB (Giovannucci et al., 2019; Pnevmatikakis et al., 2016; Zhou et al., 2018), was used to extract fluorescent calcium signals. We manually added additional seeds as necessary based on the correlation image calculated by the correlation of neighboring pixels of calcium images. Calcium traces (ΔF/F) and referred events were calculated using the functions of CaImAn toolbox. For each neuron, the amplitude of calcium traces was normalized to the maximum of ΔF/F values, and then the normalized values were summed up and divided by the number of seconds of imaging to obtain the average $Ca^{2}+$ signal per second (referred to as “area under curve per second”, or AUC/s). To calculate frequency, the calcium events for each neuron were calculated by widely used deconvolution method (Friedrich et al., 2017), and binarized with a threshold of 5 standard deviations, and then the averaged event numbers per second were calculated.

Identification of hypoactive, intermediate, and hyperactive neurons (Figs. 2 and 3): For each neuron, the averaged AUC/s during the H stage was calculated. A neuron was defined as hypoactive neuron if its averaged AUC/s value was less than 0.05 per second. A neuron was defined as hyperactive neuron if its averaged AUC/s value was greater than 0.5 per second. The rest of the neurons were defined as neurons with intermediate activity.

Data analysis for longitudinal in vivo imaging studies (Fig. 4): *In vivo* calcium imaging recorded from all control and KO mice during 5–8 independent social behavior tests ranging from 86 to 391 days post viral injection were used for analysis. To monitor the dynamic changes in neuronal activity over time, the entire field of view (650 μm × 650 μm) from each mouse was divided into 10 × 10 small sub-areas. Each subarea (65 μm × 65 μm) typically contained 5–15 active neurons which were spatially closed to each other. AUC/s during the H stage was first calculated for each neuron. Subsequently, for each small sub-area, the regional AUC/s was calculated at each imaging time point using the averaged AUC/s from the group neurons within the small sub-area. Sub-areas containing less than 3 active neurons were excluded from the regional AUC/s calculation. Sub-areas with regional AUC/s values for less than three independent time points were also excluded from the analysis. To quantify the regional AUC/s changes over time, we collectively compared the regional AUC/s values from all sub-areas at three different time periods: (1) Early: 75–125 days post viral injection;

(2) Intermediate: 125–250 days post viral injection; and (3) Late: 250–300 days post viral injection.

2.7. Brain tissue harvesting, immunostaining and confocal microscopy imaging

When the imaging field appeared to be dark and no active neurons could be detected, we harvested the brain tissue. Occasionally, the dental cement that secures the GRIN lens to mouse skull fell off and we harvested the brain tissue. The investigators who collected in vivo calcium imaging data and harvested tissues were blind regarding CTRL and KO. To harvest the brain tissues, the control and KO mice were anesthetized with overdosed Ketamine/Xylazine (Ketamine: 250 mg/kg; Xylazine: 37.5 mg/kg) and perfused with 20 mL of phosphate-buffered saline (PBS) followed by 20 mL of 4 % paraformaldehyde (PFA) in PBS. The brains were then post-fixed by 4 % PFA in PBS overnight and stored in PBS at 4 °C. The fixed mouse brains were sectioned using a vibratome (Leica VT1200S) and 60 μm thick coronal sections were collected in 24-well plates containing PBS.

TDP-43 and NeuN immunostaining: To confirm TDP-43 knockdown and possible neuron loss, immunostaining was performed using anti-TDP43 and anti-NeuN antibodies. The free-floating brain slices were washed in PBS (3 times for 5 min each) and incubated in a blocking buffer containing 1% bovine serum albumin, 4% normal donkey serum and 0.3 % Triton X-100 in PBS for 2 h at room temperature. The slices were incubated with a primary antibody solution containing mouse monoclonal anti-NeuN antibody (1B7, Abcam, 1:1000 diluted in blocking buffer) and rabbit polyclonal anti-TDP-43 antibody (10782–2-AP, Proteintech, 1:500 diluted in blocking buffer) overnight at 4 °C. The slices were washed with PBS (5 times for 5 min each) and incubated with a secondary antibody solution containing 1:300 diluted Donkey anti-Mouse IgG conjugated with Cy5 (715–175–150, Jackson ImmunoResearch Laboratories) and 1:600 diluted Donkey anti-Rabbit IgG conjugated with Alexa Fluor 594 (711–585–152, Jackson ImmunoResearch Laboratories) for 2 h at room temperature. After washing with PBS (5 times for 5 min each), the slices were mounted using antifading mounting medium with DAPI (Vector Laboratories) on slides for fluorescence imaging.

TDP-43 and Cre immunostaining: To estimate TDP-43 knockdown efficiency by AAV1-CaMKII-Cre virus, immunostaining was performed using anti-TDP43 and anti-Cre antibodies. 1:1000 diluted mouse monoclonal Cre antibody (MAB3120, Sigma-Aldrich) and 1:500 diluted rabbit polyclonal anti-TDP-43 antibody (10782–2-AP, Proteintech) in blocking buffer were used as primary antibodies. 1:300 diluted Donkey anti-Mouse IgG conjugated with Cy5 (715–175–150, Jackson ImmunoResearch Laboratories) and 1:600 diluted Donkey anti-Rabbit IgG conjugated with Alexa Fluor 594 (711–585–152, Jackson ImmunoResearch Laboratories) in blocking buffer were used as secondary antibodies.

Glial fibrillary acidic protein (GFAP) immunostaining: Immunostaining for GFAP was performed to stain the reactive astrocytes. 1:400 diluted rabbit anti-GFAP monoclonal antibody (MA5–33059, Invitrogen) was used as the primary antibody and 1:600 diluted Donkey anti-Rabbit IgG conjugated with Alexa Fluor 594 (711–585–152, Jackson ImmunoResearch Laboratories) as the secondary antibody. Density of GFAP positive cells

for the control and KO groups were determined using QuPath (https://qupath.github.io) in the virus injected and non-injected regions.

Microglial and caspase immunostaining: 1:500 diluted mouse monoclonal caspase 3 antibody (sc-136219, Santa Cruz Biotechnology) and 1:300 diluted rabbit polyclonal Iba1 (10904–1-AP, Proteintech) in blocking buffer were used as primary antibodies. 1:300 diluted Donkey anti-Mouse IgG conjugated with Cy5 (715–175–150, Jackson ImmunoResearch Laboratories) and 1:600 diluted Donkey anti-Rabbit IgG conjugated with Alexa Fluor 594 (711–585–152, Jackson ImmunoResearch Laboratories) in blocking buffer were used as secondary antibodies.

Confocal imaging: Whole brain images were taken using a 2.5X objective to locate the prelimbic region and tile images of the prelimbic region were taken using a 20X objective using a laser scanning confocal microscope (ZEISS LSM 980). Excitation lasers of 405 nm, 488 nm, 561 nm, and 639 nm were used for DAPI, GCaMP6f, Alexa Fluor 594 and Cy5, respectively. The detection wavelengths used for DAPI, GCaMP6f, Alexa Fluor 594 and Cy5 were 410–499 nm, 511–590 nm, 596–652 nm and 652–750 nm, respectively.

2.8. Nissl staining and imaging

Mouse brain sections were placed in gelatin-coated slides and allowed to dry overnight. The slides were washed in PBS (2 times, 5 min each) and rinsed in deionized water for 1 min. The slides were dipped in 1:10 diluted cresyl violet (Abcam) solution in water at room temperature for 20 min. The slides were washed with double deionized water (2 times, 5 min each). The slides were then sequentially placed in 90 % ethanol, 95 % ethanol and two changes of 100% ethanol for 3 min each. The slides were finally dipped in 100 % xylene (2 times, 3 min each). The sections were mounted in Permount mounting medium (Fisher Chemical) for imaging. Images were taken using a slide scanner (ZEISS Axio Scan Z.1) at 20X objective.

2.9. Quantification for immunostaining and Nissl staining

To quantify TDP-43, NeuN, caspase-3 and Iba1 immunostaining, QuPath was used to measure the numbers of positively stained particles within the virus injected regions (containing GCaMP6f signal) and non-injected regions (no GCaMP6f signal), respectively. The ratios of particle density between the virus injected and non-injected regions for TDP-43, NeuN, caspase-3 and Iba1 were determined and compared between the control and KO groups.

To quantify GFAP immunostaining, QuPath was used to measure the densities of positively stained particles within the virus injected regions and non-injected regions, respectively. The particle densities were compared between virus injected and non-injected regions in CTRL and KO groups.

To quantify the TDP-43 knockdown efficiency by AAV1-CaMKII-Cre virus, QuPath was used to measure the numbers of Cre and TDP-43 positively stained particles within the virus injected regions (containing GCaMP6f signal). The differences were calculated in percentage.

To quantify Nissl stained images, neuronal and glial count was determined using QuPath based on different sizes of nuclei. Nissl staining stains nuclei of both neurons and glia, but the neuronal and glial nuclei differ significantly in both shapes and size based on the Nissl staining (Sherwood et al., 2006). After multiple trials, it was determined that the sizes of neuronal nuclei fall into 40–100 μm^2, and the glial nuclei fall into 5–35 μm^2. This parameter was used to differentiate neuronal and glial cells. Nuclei detection was set automatically and all counting was done blindly. The ratios of neuron or glial density in the virus injected and non-injected regions were determined and compared between the control and KO groups.

2.10. Statistical analysis

All values in the text and Figure legends are represented as mean ± SEM. In Fig. 1B, Fig. 5A, B, and Supplementary Fig. S5B, nonparametric statistics Mann-Whitney test was used for statistical analysis between two groups. In Fig. 1C, D, and Fig. 2B, nonparametric statistics Kolmogorov-Smirnov test was used for statistical analysis between two groups. In Fig. 4C, Wilcoxon matched-pairs signed rank test was used for statistical analysis between two groups. In Fig. 5C and Supplementary Fig. S5C, nonparametric statistics Kruskal-Wallis test and Dunn's post hoc test, were used for statistical comparison among more than two groups of data. A p value less than 0.05 was considered statistically significant.

In Fig. 1E, a two-way repeated measures ANOVA was performed to evaluate the effect of different treatments (KO and CTRL) over time (H and SB) on calcium event frequency or AUC/s, since the calcium event frequency and AUC/s were recorded and calculated at two time points: H and SB. For the treatment effect, a p value less than 0.05 was considered statistically significant.

In Supplementary Figs. S2–5, we conducted a two-level analysis to compare calcium event frequency or AUC/s to address subject heterogeneity, since we observed neural activity heterogeneity across subjects (Supplementary Fig. S6). Let Y denote an outcome variable of interest (i.e., calcium event frequency or AUC/s). The procedure was carried as follows. First, we transformed Y for normality by applying a square root because the raw Y was highly skewed. Second, we performed a subject-level analysis. We compared each KO subject's Y with that of the CTRL subject. There were 10 KO subjects and 8 CTRL subjects. And we performed 8 × 10 = 80 comparisons. Third, we used a meta-analysis method, random effects model, to aggregate the findings from these comparisons. The standardized mean difference was used as a summary statistic in the meta-analysis.

3. Results

3.1. TDP-43 deletion in excitatory neurons of the PFC initially leads to hyperactive calcium activity

We bilaterally injected adeno-associated viruses (AAVs) expressing Cre recombinase driven by the CaMKII promoter (AAV1-CaMKII-Cre) and a Cre-dependent GCaMP6f (a genetically encoded green fluorescent calcium indicator) in the medial prefrontal cortex (PFC) of young adult (i.e., 3–4 months old) *Tdp-43*$^{F/F}$ mice (Chiang et al., 2010), to selectively delete TDP-43 and express GCaMP6f in pyramidal neurons in the PFC (Fig.

1A, referred to as KO mice). In parallel, we injected AAV-CaMKII-GCaMP6f virus to the PFC of young adult *Tdp-43*$^{F/F}$ mice to express GCaMP6f in pyramidal neurons (Fig. 1A, referred to as CTRL mice). Therefore, GCaMP6f labeled TDP-43 deleted pyramidal neurons in KO mice, whereas labeled TDP-43 intact pyramidal neurons in control (CTRL) mice. We then implanted a 1-mm diameter gradient index (GRIN) lens into the PFC of these KO and CTRL mice. *Via* a custom-built miniscope recording system (Barbera et al., 2016; Liang et al., 2018; Zhang et al., 2021), we performed in vivo calcium imaging during a 20-minute social behavior test containing two stages (10-minute each), namely, habituation (H) and sociability (SB). We found that KO mice exhibited normal sociability, like that of CTRL mice (Fig. 1B).

We used a MATLAB calcium imaging process toolbox, CaImAn (Giovannucci et al., 2019), to identify active neurons and extract fluorescence changes (ΔF/F) of GCaMP6f from cell bodies of these neurons as somatic calcium activity (Supplementary Fig. S1). For each active neuron, the amplitude of calcium trace was normalized to the maximum of absolute ΔF/F value. The frequency of calcium events, as well as the average of normalized ΔF/F values over time (referred to as "area under curve per second", or AUC/s), were calculated and compared between CTRL and KO groups. We found that neurons in KO mice exhibited significant increases in calcium event frequency (Fig. 1C and Supplementary Figs. S2–S3) and AUC/s (Fig. 1D and Supplementary Figs. S4–S5) during each 10-minute stage (n = 2355 and n = 2828 neurons for CTRL and KO groups at H stage; n = 2364 and n = 2842 neurons for CTRL and KO groups at H stage; Kolmogorov-Smirnov test, $p < 0.0001$). We next calculated the averaged calcium event frequency and AUC/s from individual mice at each behavioral stage and found that the KO group exhibited significantly higher calcium event frequency and AUC/s than those of the CTRL group (n = 8 and n = 10 mice for CTRL and KO groups. Calcium event frequency for CTRL mice at H and SB stages: 0.046 ± 0.004 and 0.041 ± 0.003 per second; calcium event frequency for KO mice at H and SB stages: 0.058 ± 0.003 and 0.054 ± 0.004 per second; AUC/s for CTRL mice at H and SB stages: 0.184 ± 0.017 and 0.168 ± 0.014 per second; AUC/s for KO mice at H and SB stages: 0.258 ± 0.022 and 0.223 ± 0.020 per second; Two-way repeated measures ANOVA, $p < 0.05$, Fig. 1E), indicating hyperactivity in PFC pyramidal neurons triggered by TDP-43 depletion.

3.2. Longitudinal in vivo calcium imaging reveals dynamic activity changes after TDP-43 deletion

We then performed in vivo calcium imaging repetitively during the social behavior test every 4–6 weeks (Fig. 2A). We successfully collected in vivo calcium imaging from four KO and four CTRL mice for up to 7 months (i.e., the first recording was performed 3 months after the viral injection, and the last recording was performed 10 months after the viral injection). We then compared the AUC/s of calcium traces during the H stage in PFC pyramidal neurons between KO and CTRL mice at the neuronal population level (Fig. 2B). We showed that KO pyramidal neurons exhibited increased AUC/s activity 3 months after TDP-43 depletion, but reduced AUC/s activity 10 months after TDP-43 depletion compared to pyramidal neurons in CTRL mice (n = 1074 and n = 1400 neurons from 4 CTRL mice and 4 KO mice at 3 months post viral injection; n = 731 and n = 256 neurons from 4 CTRL mice and 4 KO mice at 10 months post viral injection. AUC/s activity from CTRL and

KO at 3 months post-virus injection: 0.205 ± 0.006 and 0.269 ± 0.009 per second; CTRL and KO at 10 months post-virus injection: 0.167 ± 0.006 and 0.108 ± 0.011 per second; Kolmogorov-Smirnov test, $p < 0.0001$).

Pyramidal neurons in the PFC display high heterogeneity in calcium activity in behaving mice (Liang et al., 2018). We next compared the distribution of the average AUC/s of calcium traces from individual PFC pyramidal neurons between KO and CTRL mice at two time points: 3 months and 10 months post viral injection. We set the thresholds to define the intermediate range (0.05–0.5 per second) of AUC/s values. Neurons displaying AUC/s values outside of the intermediate range were referred to as either hypoactive or hyperactive neurons (Fig. 2C, also see Supplementary Fig. S6). Among pyramidal neurons from CTRL mice, while the majority displayed intermediate calcium activity, there were less than 10 % of neurons displaying hyperactivity, and less than 20 % of neurons displaying hypoactivity at both time points (top panels in Fig. 2C and 2D). Interestingly, 3 months after TDP-43 depletion, there were two-fold increases in percentage of neurons displaying hyperactivity from the KO mice (16 % in KO, bottom panel in Fig. 2C) than that of CTRL mice (8 % in CTRL, top panel in Fig. 2C). By contrast, 10 months after TDP-43 depletion, there were almost three times as many hypoactive neurons observed in KO mice (54 % in KO, bottom panel in Fig. 2D) as that of CTRL mice (19 % in CTRL, top panel in Fig. 2D).

We also showed cell activity maps indicating hypoactive, intermediate, and hyperactive pyramidal neurons, from representative KO mice and CTRL mice at different time points following TDP-43 depletion (Fig. 3 and Supplementary Fig. S7). In most cases for the CTRL mice, the total detectable active neurons were slightly reduced with time probably due to the reduced viral expression of GCaMP6f. Nevertheless, the CTRL mice exhibited a relatively stable activity pattern across different time points (e.g., similar proportion of hyperactive and hypoactive neurons over time). In contrast, the KO mice exhibited substantial changes in neuronal calcium activity following viral injection, and in some cases, even drastic loss of detectable active neurons.

3.3. Rapid activity decline associated with long term TDP-43 depletion

To monitor the dynamic changes in neuronal calcium activity during disease progression, an ideal approach is to follow individual neurons to monitor their dynamics over time. However, since intervals between our repetitive in vivo calcium imaging were 30–45 days, it was difficult to accurately identify the exact same neurons on cell maps recorded at different time points. As a practical substitute, we divided each imaged PFC brain region into multiple small sub-areas (size: 65 μm by 65 μm) where a small group (typically 5–15) of spatially adjacent neurons can be identified (Fig. 4A). We selected those sub-areas containing at least 3 neurons to measure their averaged AUC/s activity and followed their activity changes over time. Starting with 175 and 285 such small sub-areas in 8 CTRL mice and 10 KO mice, respectively, we plotted the time course of activity changes from the same sub-areas across disease progression (Fig. 4B). We found that most CTRL mice displayed relatively stable activity over the time course of 7 months, whereas most KO mice displayed rapid activity declines over time. We further quantified the averaged AUC/s from individual mice during disease progression at three time periods: 75–125 days, 125–250 days, and

250–300 days post viral injection, referred to as early, intermediate and late stages (Fig. 4C). We confirmed that the CTRL group displayed a constant AUC/s activity across time (0.199 ± 0.020, 0.174 ± 0.025, and 0.166 ± 0.019 per second; n = 8, 8, and 4 mice for early, intermediate and late stages; Wilcoxon matched-pairs signed rank test for early vs intermediate, p = 0.84), while the KO group showed dynamic activity changes, a rapidly reduced AUC/s activity following the initial hyperactivity (0.236 ± 0.032, 0.142 ± 0.015, and 0.176 ± 0. 017 per second; n = 9, 9, 2 mice for early, intermediate and late stages; Wilcoxon matched-pairs signed rank test for early vs intermediate, $p < 0.01$). These data suggest that long term depletion of TDP-43 in the PFC causes a rapid activity decline in pyramidal neurons.

3.4. Immunohistochemistry analysis reveals neuron loss and gliosis

We harvested brain tissues after the very last in vivo calcium imaging and performed a series of immunohistochemistry studies (Fig. 5). We first confirmed TDP-43 depletion in the KO brain tissues and demonstrated that the knockout efficiency of the AAV-CaMKII-Cre virus was 86.96 % (n = 16 counts from both sides of 8 brain sections, Supplementary Fig. S8). We further demonstrated that TDP-43 depletion was accompanied by a significant reduction in NeuN staining (n = 49 and n = 75 brain sections for CTRL and KO groups; ratios for TDP-43 staining in CRTL and KO groups: 1.00 ± 0.07 and 0,54 ± 0.03; ratios for NeuN staining in CRTL and KO groups: 1.00 ± 0.16 and 0.63 ± 0.05; Mann-Whitney test, $p < 0.0001$; Fig. 5A). We then performed Nissl stain and compared neuronal and glial cell densities between CTRL and KO groups. In Nissl stained sections, neurons can be distinguished from glial cells by their different staining patterns and sizes. Neurons typically display larger stained nuclei and lightly stained proximal segments of dendritic processes, while glial cells contain less stained endoplasmic reticulum and smaller nuclei (Sherwood et al., 2006). Therefore, the parameters for glial and neuronal nuclei were set as 5–35 μm^2 and 40–100 μm^2, respectively. Nuclei detection was performed automatically, and neuronal and glial counting was done blindly across all brain sections. The ratios of neuronal and glial density at the virus injected and non-injected areas were determined and compared between the CTRL and KO groups. Within the virus injected areas of KO mice, there were significantly reduced neurons (n = 15 and n = 18 brain sections for CTRL and KO groups; ratios in CTRL and KO: 1.16 ± 0.06 and 0.92 ± 0.05, Mann-Whitney test, $p < 0.01$), yet significantly increased glial cells (ratios in CTRL and KO: 1.11 ± 0.05 and 1.31 ± 0.06, Mann-Whitney test, $p < 0.05$) than those of CTRL mice (Fig. 5B). GFAP staining further revealed that virus injected areas in KO mice exhibited substantially more GFAP signals than that of CTRL mice (n = 18 and n = 24 brain sections for CTRL and KO groups; non-injected and virus injected CTRL: 21.4 ± 5.9 and 100.0 ± 34.8; non-injected and virus injected KO: 89.7 ± 22.2 and 1257.0 ± 131.7; Kruskal-Wallis test, $p < 0.0001$; Dunn's post hoc test, virus injected KO vs any of the other three groups, $p < 0.0001$; Fig. 5C). Microglial staining did not show a statistically significant difference between CTRL and KO groups (n = 10 and n = 13 brain sections for CTRL and KO groups; ratios in CTRL and KO: 1.89 ± 0.35 and 2.31 ± 0.35, Mann-Whitney test, p = 0.45; Supplementary Fig. S9, panels A and B). Caspase 3 staining revealed an increase in caspase positive particles in virus injected areas of KO mice (n = 10 and n = 13 brain sections for CTRL and KO groups; non-injected and virus injected CTRL: 0.0 ± 0.0 and 46.2 ± 37.4; non-injected and virus injected KO: 0.9

± 0.9 and 151.6 ± 80.5; Kruskal-Wallis test, $p < 0.0001$; Dunn's post hoc test, virus injected KO vs virus injected CTRL, $p < 0.05$; Supplementary Fig. S9, panels A and C), indicating an ongoing apoptosis associated with loss of TDP-43. Together, these results support the idea that TDP-43 depletion causes aberrant neural activity of pyramidal neurons in the PFC that ultimately leads to gliosis and neuron loss.

4. Discussion

Our longitudinal in vivo calcium imaging studies from awake behaving mice demonstrated aberrant calcium activity in PFC pyramidal neurons prior to neurodegeneration driven by TDP-43 loss-of-function. In particular, we observed that TDP-43 depletion in pyramidal neurons of the PFC triggered an initial hyperactivity followed by a rapid activity decline during early disease progression.

It has long been proposed that excitotoxicity, typically from excessive and prolonged activation of glutamate receptors, is the primary driving force for neurodegenerative disorders such as ALS (King et al., 2016). Changes in intrinsic excitability which could lead to excitotoxicity, namely hyperexcitability, have been recognized as an early pathological sign in ALS. For instance, cortical hyperexcitability is well documented in transcranial magnetic stimulation (TMS) studies with ALS patients (Vucic and Kiernan, 2013; Williams et al., 2013). Hyperexcitability has also been reported in cortical motor neurons of ALS mouse models (Kim et al., 2017; Pieri et al., 2003, 2009; Saba et al., 2016). In addition, multiple lines of motor neurons derived from patient induced pluripotent stem cell (iPSC) harboring mutations in superoxide dismutase 1 (*SOD1)*, fused-in-sarcoma (*FUS)*, *TDP-43*, or *C9ORF72*, displayed hyperexcitability relative to healthy motor neurons (Huang et al., 2021; Wainger et al., 2014).

In contrast, some studies failed to observe hyperexcitability in spinal motor neurons of ALS rodent models, instead reported hypoexcitability in a substantial number of spinal motor neurons before denervation (Delestree et al., 2014). Again, other iPSC studies reported hypoexcitability displayed by motor neurons derived from patients with *C9ORF72* or *FUS* mutations (Guo et al., 2017; Sareen et al., 2013). Therefore, hypoexcitability has also been proposed as a marker of disease progression in ALS. Moreover, some studies reported transient hyperexcitability followed by a progressive activity loss in iPSC-derived motor neurons from patients with *TDP-43* or *C9ORF72* mutations (Devlin et al., 2015).

Consistent with these previous reports using iPSC models, here we observed biphasic activity changes in neuronal calcium activity triggered by TDP-43 depletion during disease progression from awake behaving mice. In sharp contrast to the relatively stable neuronal calcium activity displayed by CTRL mice, TDP-43 depletion in PFC excitatory neurons leads to an initial hyperactivity followed by a rapid activity decline prior to neuron loss, emphasizing the important role of aberrant neural activity during early stage of the neurodegenerative process. Neuronal hypoactivity following hyperactivity could result from activation of cell intrinsic compensatory mechanism or network compensatory effect from GABAergic inhibition (Palop et al., 2007). Dynamic changes in neuronal calcium activity triggered by TDP-43 loss-of-function strongly indicate that disruptive and imbalanced

calcium homeostasis might be involved in the initiation and downstream pathways that ultimately lead to neurodegeneration in FTD and ALS.

As a ubiquitous second messenger, calcium plays important roles in a variety of cellular processes, from neuronal excitation to synaptic communication. Dysfunctions in cellular calcium homeostasis have been suggested as one of the primary driving forces in neurodegenerative disorders such as AD (Magi et al., 2016; Marambaud et al., 2009). Elevated resting intracellular calcium level has been reported in cortical neurons of a transgenic AD mouse model (Lopez et al., 2008). With two-photon calcium imaging, hyperactive neurons and calcium overloaded neurites were found in proximity of β-amyloid plaques in transgenic AD mouse models (Busche et al., 2008; Kuchibhotla et al., 2008). Moreover, it was reported that direct application of soluble β-amyloid was capable of inducing hyperactive calcium activity in even wildtype mice (Busche et al., 2012).

Interestingly, abnormal intracellular calcium has also been reported in various ALS models carrying TDP-43 mutants. For instance, in motor neurons of a *C. elegans* model, elevated intracellular calcium has been suggested as a driver of mutant TDP-43 mediated neuronal toxicity (Aggad et al., 2014). Patients-derived motor neurons harboring TDP-43 mutations displayed high glutamate-induced calcium release (Dafinca et al., 2020). In a *Drosophila* model, deficits in motor functions mediated by TDP-43 mutants can be rescued by genetically restoring a voltage-gated calcium channel (Lembke and Morton, 2017).

Here using in vivo calcium imaging from awake behaving mice, we observed dynamic activity changes in PFC pyramidal neurons upon TDP-43 depletion during disease progression. Particularly, TDP-43 depletion triggers initial hyperactivity followed by a rapid decline in calcium activity. Given that TDP-43 plays important roles in RNA splicing, RNA transport and RNA stabilization, TDP-43 depletion might affect intracellular calcium signaling by directly interfering with intrinsic excitability and/or calcium homeostasis pathways. The possible causes of aberrant calcium activity triggered by loss of TDP-43 could be excessive activation of glutamate receptors, dysregulation in calcium channels, weakening of calcium buffering capacities, or disruptions in mitochondrial and endoplasmic reticulum calcium homeostasis (Marambaud et al., 2009). Alternatively, it is also possible that neuronal calcium hyperactivity may be a phenomenon caused by a neuron at the early stages towards cell death running out of energy to support the expensive calcium homeostasis without direct influence of any calcium related molecules and pathways triggered by TDP-43 depletion. Follow-up studies will be needed to dissect out major players regarding calcium dysfunctions triggered by TDP-43 depletion.

5. Conclusions

TDP-43 depletion in excitatory neurons of the PFC leads to initial hyperactivity followed by a rapid activity decline in excitatory neurons of the PFC, before the ultimate loss of neurons.

Supplementary Material

Refer to Web version on PubMed Central for supplementary material.

Acknowledgments

We would like to thank the IMCore/Microscopy facility at the University of Wyoming.

Funding

This work was supported by the National Institutes of Health [5P20GM121310, R61NS115161, and UG3NS115608]; and the intramural research program (IRP) at the National Institute on Drug Abuse (NIDA).

Abbreviations:

TDP-43	TAR DNA binding protein 43 kDa, or TARDBP-43
ALS	amyotrophic lateral sclerosis
FTD	frontotemporal dementia
AD	Alzheimer's disease
hnRNPs	heterogeneous nuclear ribonucleoproteins
Miniscope	miniature fluorescence microscope
PFC	prefrontal cortex
ACSF	artificial cerebrospinal fluid
GFAP	glial fibrillary acidic protein
AAV	adeno-associated virus
GRIN lens	gradient index lens
CTRL	control
KO	knockout
AUC/s	area under curve per second
TMS	transcranial magnetic stimulation
iPSC	induced pluripotent stem cell
SOD1	superoxide dismutase 1
FUS	fused-in-sarcoma

References

Aggad D, Veriepe J, Tauffenberger A, Parker JA, 2014. TDP-43 toxicity proceeds via calcium dysregulation and necrosis in aging Caenorhabditis elegans motor neurons. J. Neurosci. 34, 12093–12103. 10.1523/JNEUROSCI.2495-13.2014. [PubMed: 25186754]

Amador-Ortiz C, Lin WL, Ahmed Z, Personett D, Davies P, Duara R, Graff-Radford NR, Hutton ML, Dickson DW, 2007. TDP-43 immunoreactivity in hippocampal sclerosis and Alzheimer's disease. Ann. Neurol. 61, 435–445. 10.1002/ana.21154. [PubMed: 17469117]

Anekonda TS, Quinn JF, 2011. Calcium channel blocking as a therapeutic strategy for Alzheimer's disease: the case for isradipine. Biochim. Biophys. Acta 1812, 1584–1590. 10.1016/j.bbadis.2011.08.013. [PubMed: 21925266]

Barbera G, Liang B, Zhang L, Gerfen CR, Culurciello E, Chen R, Li Y, Lin DT, 2016. Spatially compact neural clusters in the dorsal striatum encode locomotion relevant information. Neuron 92, 202–213. 10.1016/j.neuron.2016.08.037. [PubMed: 27667003]

Borroni B, Bonvicini C, Alberici A, Buratti E, Agosti C, Archetti S, Papetti A, Stuani C, Di Luca M, Gennarelli M, Padovani A, 2009. Mutation within TARDBP leads to frontotemporal dementia without motor neuron disease. Hum. Mutat. 30, E974–E983. 10.1002/humu.21100. [PubMed: 19655382]

Brown A-L, Wilkins OG, Keuss MJ, Hill SE, Zanovello M, Lee WC, Lee FCY, Masino L, Qi YA, Bryce-Smith S, et al. , 2021. Common ALS/FTD risk variants in UNC13A exacerbate its cryptic splicing and loss upon TDP-43 mislocalization. bioRxiv 603, 131–137. 10.1101/2021.04.02.438170.

Buratti E, Brindisi A, Giombi M, Tisminetzky S, Ayala YM, Baralle FE, 2005. TDP-43 binds heterogeneous nuclear ribonucleoprotein A/B through its C-terminal tail: an important region for the inhibition of cystic fibrosis transmembrane conductance regulator exon 9 splicing. J. Biol. Chem. 280, 37572–37584. 10.1074/jbc.M505557200. [PubMed: 16157593]

Busche MA, Eichhoff G, Adelsberger H, Abramowski D, Wiederhold KH, Haass C, Staufenbiel M, Konnerth A, Garaschuk O, 2008. Clusters of hyperactive neurons near amyloid plaques in a mouse model of Alzheimer's disease. Science 321, 1686–1689. 10.1126/science.1162844. [PubMed: 18802001]

Busche MA, Chen X, Henning HA, Reichwald J, Staufenbiel M, Sakmann B, Konnerth A, 2012. Critical role of soluble amyloid-beta for early hippocampal hyperactivity in a mouse model of Alzheimer's disease. Proc. Natl. Acad. Sci. USA 109, 8740–8745. 10.1073/pnas.1206171109. [PubMed: 22592800]

Chiang PM, Ling J, Jeong YH, Price DL, Aja SM, Wong PC, 2010. Deletion of TDP-43 down-regulates Tbc1d1, a gene linked to obesity, and alters body fat metabolism. Proc. Natl. Acad. Sci. USA 107, 16320–16324. 10.1073/pnas.1002176107. [PubMed: 20660762]

Dafinca R, Barbagallo P, Farrimond L, Candalija A, Scaber J, Ababneh NA, Sathyaprakash C, Vowles J, Cowley SA, Talbot K, 2020. Impairment of mitochondrial calcium buffering links mutations in C9ORF72 and TARDBP in iPS-derived motor neurons from patients with ALS/FTD. Stem Cell Rep. 14, 892–908. 10.1016/j.stemcr.2020.03.023.

Delestree N, Manuel M, Iglesias C, Elbasiouny SM, Heckman CJ, Zytnicki D, 2014. Adult spinal motoneurones are not hyperexcitable in a mouse model of inherited amyotrophic lateral sclerosis. J. Physiol. 592, 1687–1703. 10.1113/jphysiol.2013.265843. [PubMed: 24445319]

Devlin AC, Burr K, Borooah S, Foster JD, Cleary EM, Geti I, Vallier L, Shaw CE, Chandran S, Miles GB, 2015. Human iPSC-derived motoneurons harbouring TARDBP or C9ORF72 ALS mutations are dysfunctional despite maintaining viability. Nat. Commun. 6, 5999. 10.1038/ncomms6999. [PubMed: 25580746]

Diaper DC, Adachi Y, Sutcliffe B, Humphrey DM, Elliott CJ, Stepto A, Ludlow ZN, Vanden Broeck L, Callaerts P, Dermaut B, et al. , 2013. Loss and gain of Drosophila TDP-43 impair synaptic efficacy and motor control leading to agerelated neurodegeneration by loss-of-function phenotypes. Hum. Mol. Genet. 22, 1539–1557. 10.1093/hmg/ddt005. [PubMed: 23307927]

Donde A, Sun M, Ling JP, Braunstein KE, Pang B, Wen X, Cheng X, Chen L, Wong PC, 2019. Splicing repression is a major function of TDP-43 in motor neurons. Acta Neuropathol. 138, 813–826. 10.1007/s00401-019-02042-8. [PubMed: 31332509]

Feiguin F, Godena VK, Romano G, D'Ambrogio A, Klima R, Baralle FE, 2009. Depletion of TDP-43 affects drosophila motoneurons terminal synapsis and locomotive behavior. FEBS Lett. 583, 1586–1592. 10.1016/j.febslet.2009.04.019. [PubMed: 19379745]

Friedrich J, Zhou P, Paninski L, 2017. Fast online deconvolution of calcium imaging data. PLOS Comput. Biol. 13, e1005423 10.1371/journal.pcbi.1005423. [PubMed: 28291787]

Giovannucci A, Friedrich J, Gunn P, Kalfon J, Brown BL, Koay SA, Taxidis J, Najafi F, Gauthier JL, Zhou P, et al. , 2019. CaImAn an open source tool for scalable calcium imaging data analysis. eLife 8. 10.7554/eLife.38173.

Guo W, Naujock M, Fumagalli L, Vandoorne T, Baatsen P, Boon R, Ordovas L, Patel A, Welters M, Vanwelden T, et al. , 2017. HDAC6 inhibition reverses axonal transport defects in motor neurons derived from FUS-ALS patients. Nat. Commun. 8, 861. 10.1038/s41467-017-00911-y. [PubMed: 29021520]

Huang X, Roet KCD, Zhang L, Brault A, Berg AP, Jefferson AB, Klug-McLeod J, Leach KL, Vincent F, Yang H, et al. , 2021. Human amyotrophic lateral sclerosis excitability phenotype screen: target discovery and validation. Cell Rep. 35, 109224 10.1016/j.celrep.2021.109224. [PubMed: 34107252]

Igaz LM, Kwong LK, Lee EB, Chen-Plotkin A, Swanson E, Unger T, Malunda J, Xu Y, Winton MJ, Trojanowski JQ, Lee VM, 2011. Dysregulation of the ALS-associated gene TDP-43 leads to neuronal death and degeneration in mice. J. Clin. Investig. 121, 726–738. 10.1172/JCI44867. [PubMed: 21206091]

Iguchi Y, Katsuno M, Niwa J, Takagi S, Ishigaki S, Ikenaka K, Kawai K, Watanabe H, Yamanaka K, Takahashi R, et al. , 2013. Loss of TDP-43 causes age-dependent progressive motor neuron degeneration. Brain 136, 1371–1382. 10.1093/brain/awt029. [PubMed: 23449777]

Janssens J, Van Broeckhoven C, 2013. Pathological mechanisms underlying TDP-43 driven neurodegeneration in FTLD-ALS spectrum disorders. Hum. Mol. Genet. 22, R77–R87. 10.1093/hmg/ddt349. [PubMed: 23900071]

Kabashi E, Valdmanis PN, Dion P, Spiegelman D, McConkey BJ, Vande Velde C, Bouchard JP, Lacomblez L, Pochigaeva K, Salachas F, et al. , 2008. TARDBP mutations in individuals with sporadic and familial amyotrophic lateral sclerosis. Nat. Genet. 40, 572–574. 10.1038/ng.132. [PubMed: 18372902]

Kim J, Hughes EG, Shetty AS, Arlotta P, Goff LA, Bergles DE, Brown SP, 2017. Changes in the excitability of neocortical neurons in a mouse model of amyotrophic lateral sclerosis are not specific to corticospinal neurons and are modulated by advancing disease. J. Neurosci. 37, 9037–9053. 10.1523/JNEUROSCI.0811-17.2017. [PubMed: 28821643]

King AE, Woodhouse A, Kirkcaldie MT, Vickers JC, 2016. Excitotoxicity in ALS: overstimulation, or overreaction? Exp. Neurol. 275 (Pt 1), 162–171. 10.1016/j.expneurol.2015.09.019. [PubMed: 26584004]

Klim JR, Williams LA, Limone F, Guerra San Juan I, Davis-Dusenbery BN, Mordes DA, Burberry A, Steinbaugh MJ, Gamage KK, Kirchner R, et al. , 2019. ALS-implicated protein TDP-43 sustains levels of STMN2, a mediator of motor neuron growth and repair. Nat. Neurosci. 22, 167–179. 10.1038/s41593-018-0300-4. [PubMed: 30643292]

Kovacs GG, Murrell JR, Horvath S, Haraszti L, Majtenyi K, Molnar MJ, Budka H, Ghetti B, Spina S, 2009. TARDBP variation associated with frontotemporal dementia, supranuclear gaze palsy, and chorea. Mov. Disord. 24, 1843–1847. 10.1002/mds.22697. [PubMed: 19609911]

Kraemer BC, Schuck T, Wheeler JM, Robinson LC, Trojanowski JQ, Lee VM, Schellenberg GD, 2010. Loss of murine TDP-43 disrupts motor function and plays an essential role in embryogenesis. Acta Neuropathol. 119, 409–419. 10.1007/s00401-010-0659-0. [PubMed: 20198480]

Kuchibhotla KV, Goldman ST, Lattarulo CR, Wu HY, Hyman BT, Bacskai BJ, 2008. Abeta plaques lead to aberrant regulation of calcium homeostasis in vivo resulting in structural and functional disruption of neuronal networks. Neuron 59, 214–225. 10.1016/j.neuron.2008.06.008. [PubMed: 18667150]

Lee EB, Lee VM, Trojanowski JQ, 2011. Gains or losses: molecular mechanisms of TDP43-mediated neurodegeneration. Nat. Rev. Neurosci. 13, 38–50. 10.1038/nrn3121. [PubMed: 22127299]

Lembke KM, Morton DB, 2017. Exploring the interaction of drosophila TDP-43 and the type II voltage-gated calcium channel, cacophony, in regulating motor function and behavior. J. Exp. Neurosci. 11 10.1177/1179069517740892.

Liang B, Zhang L, Barbera G, Fang W, Zhang J, Chen X, Chen R, Li Y, Lin DT, 2018. Distinct and dynamic ON and OFF neural ensembles in the prefrontal cortex code social exploration. Neuron 100, 700–714. 10.1016/j.neuron.2018.08.043. [PubMed: 30269987]

Liang B, Zhang L, Moffitt C, Li Y, Lin DT, 2019. An open-source automated surgical instrument for microendoscope implantation. J. Neurosci. Methods 311, 83–88. 10.1016/j.jneumeth.2018.10.013. [PubMed: 30326202]

Ling JP, Pletnikova O, Troncoso JC, Wong PC, 2015. TDP-43 repression of nonconserved cryptic exons is compromised in ALS-FTD. Science 349, 650–655. 10.1126/science.aab0983. [PubMed: 26250685]

Ling SC, Polymenidou M, Cleveland DW, 2013. Converging mechanisms in ALS and FTD: disrupted RNA and protein homeostasis. Neuron 79, 416–438. 10.1016/j.neuron.2013.07.033. [PubMed: 23931993]

Lopez JR, Lyckman A, Oddo S, Laferla FM, Querfurth HW, Shtifman A, 2008. Increased intraneuronal resting [Ca2+] in adult Alzheimer's disease mice. J. Neurochem. 105, 262–271. 10.1111/j.1471-4159.2007.05135.x. [PubMed: 18021291]

Ma XR, Prudencio M, Koike Y, Vatsavayai SC, Kim G, Harbinski F, Rodriguez CM, Schmidt HB, Cummings BB, Wyatt DW, et al. , 2021. TDP-43 represses cryptic exon inclusion in FTD/ALS gene UNC13A. bioRxiv 603, 124–130. 10.1101/2021.04.02.438213.

Magi S, Castaldo P, Macri ML, Maiolino M, Matteucci A, Bastioli G, Gratteri S, Amoroso S, Lariccia V, 2016. Intracellular calcium dysregulation: implications for Alzheimer's disease. Biomed. Res. Int. 2016, 6701324 10.1155/2016/6701324. [PubMed: 27340665]

Marambaud P, Dreses-Werringloer U, Vingtdeux V, 2009. Calcium signaling in neurodegeneration. Mol. Neurodegener. 4, 20. 10.1186/1750-1326-4-20. [PubMed: 19419557]

Melamed Z, Lopez-Erauskin J, Baughn MW, Zhang O, Drenner K, Sun Y, Freyermuth F, McMahon MA, Beccari MS, Artates JW, et al. , 2019. Premature polyadenylation-mediated loss of stathmin-2 is a hallmark of TDP-43-dependent neurodegeneration. Nat. Neurosci. 22, 180–190. 10.1038/s41593-018-0293-z. [PubMed: 30643298]

Nana AL, Sidhu M, Gaus SE, Hwang JL, Li L, Park Y, Kim EJ, Pasquini L, Allen IE, Rankin KP, et al. , 2019. Neurons selectively targeted in frontotemporal dementia reveal early stage TDP-43 pathobiology. Acta Neuropathol. 137, 27–46. 10.1007/s00401-018-1942-8. [PubMed: 30511086]

Neumann M, Sampathu DM, Kwong LK, Truax AC, Micsenyi MC, Chou TT, Bruce J, Schuck T, Grossman M, Clark CM, et al. , 2006. Ubiquitinated TDP-43 in frontotemporal lobar degeneration and amyotrophic lateral sclerosis. Science 314, 130–133. 10.1126/science.1134108. [PubMed: 17023659]

Palop JJ, Chin J, Roberson ED, Wang J, Thwin MT, Bien-Ly N, Yoo J, Ho KO, Yu GQ, Kreitzer A, et al. , 2007. Aberrant excitatory neuronal activity and compensatory remodeling of inhibitory hippocampal circuits in mouse models of Alzheimer's disease. Neuron 55, 697–711. 10.1016/j.neuron.2007.07.025. [PubMed: 17785178]

Pieri M, Albo F, Gaetti C, Spalloni A, Bengtson CP, Longone P, Cavalcanti S, Zona C, 2003. Altered excitability of motor neurons in a transgenic mouse model of familial amyotrophic lateral sclerosis. Neurosci. Lett. 351, 153–156. 10.1016/j.neulet.2003.07.010. [PubMed: 14623129]

Pieri M, Carunchio I, Curcio L, Mercuri NB, Zona C, 2009. Increased persistent sodium current determines cortical hyperexcitability in a genetic model of amyotrophic lateral sclerosis. Exp. Neurol. 215, 368–379. 10.1016/j.expneurol.2008.11.002. [PubMed: 19071115]

Pnevmatikakis EA, Giovannucci A, 2017. NoRMCorre: an online algorithm for piecewise rigid motion correction of calcium imaging data. J. Neurosci. Methods 291, 83–94. [PubMed: 28782629]

Pnevmatikakis EA, Soudry D, Gao Y, Machado TA, Merel J, Pfau D, Reardon T, Mu Y, Lacefield C, Yang W, et al. , 2016. Simultaneous denoising, deconvolution, and demixing of calcium imaging data. Neuron 89, 285–299. 10.1016/j.neuron.2015.11.037. [PubMed: 26774160]

Polymenidou M, Lagier-Tourenne C, Hutt KR, Huelga SC, Moran J, Liang TY, Ling SC, Sun E, Wancewicz E, Mazur C, et al. , 2011. Long pre-mRNA depletion and RNA missplicing contribute to neuronal vulnerability from loss of TDP-43. Nat. Neurosci. 14, 459–468. 10.1038/nn.2779. [PubMed: 21358643]

Ritson GP, Custer SK, Freibaum BD, Guinto JB, Geffel D, Moore J, Tang W, Winton MJ, Neumann M, Trojanowski JQ, et al. , 2010. TDP-43 mediates degeneration in a novel Drosophila model of disease caused by mutations in VCP/p97. J. Neurosci. 30, 7729–7739. 10.1523/JNEUROSCI.5894-09.2010. [PubMed: 20519548]

Saba L, Viscomi MT, Caioli S, Pignataro A, Bisicchia E, Pieri M, Molinari M, Ammassari-Teule M, Zona C, 2016. Altered functionality, morphology, and vesicular glutamate transporter expression

of cortical motor neurons from a presymptomatic mouse model of amyotrophic lateral sclerosis. Cereb. Cortex 26, 1512–1528. 10.1093/cercor/bhu317. [PubMed: 25596588]

Sareen D, O'Rourke JG, Meera P, Muhammad AK, Grant S, Simpkinson M, Bell S, Carmona S, Ornelas L, Sahabian A, et al. , 2013. Targeting RNA foci in iPSC-derived motor neurons from ALS patients with a C9ORF72 repeat expansion. Sci. Transl. Med. 5 10.1126/scitranslmed.3007529.

Schmid B, Hruscha A, Hogl S, Banzhaf-Strathmann J, Strecker K, van der Zee J, Teucke M, Eimer S, Hegermann J, Kittelmann M, et al. , 2013. Loss of ALS-associated TDP-43 in zebrafish causes muscle degeneration, vascular dysfunction, and reduced motor neuron axon outgrowth. Proc. Natl. Acad. Sci. USA 110, 4986–4991. 10.1073/pnas.1218311110. [PubMed: 23457265]

Sephton CF, Good SK, Atkin S, Dewey CM, Mayer P 3rd, Herz J, Yu G, 2010. TDP-43 is a developmentally regulated protein essential for early embryonic development. J. Biol. Chem. 285, 6826–6834. 10.1074/jbc.M109.061846. [PubMed: 20040602]

Sherwood CC, Stimpson CD, Raghanti MA, Wildman DE, Uddin M, Grossman LI, Goodman M, Redmond JC, Bonar CJ, Erwin JM, Hof PR, 2006. Evolution of increased glia-neuron ratios in the human frontal cortex. Proc. Natl. Acad. Sci. USA 103, 13606–13611. 10.1073/pnas.0605843103. [PubMed: 16938869]

Sreedharan J, Blair IP, Tripathi VB, Hu X, Vance C, Rogelj B, Ackerley S, Durnall JC, Williams KL, Buratti E, et al. , 2008. TDP-43 mutations in familial and sporadic amyotrophic lateral sclerosis. Science 319, 1668–1672. 10.1126/science.1154584. [PubMed: 18309045]

Stallings NR, Puttaparthi K, Luther CM, Burns DK, Elliott JL, 2010. Progressive motor weakness in transgenic mice expressing human TDP-43. Neurobiol. Dis. 40, 404–414. 10.1016/j.nbd.2010.06.017. [PubMed: 20621187]

Styr B, Slutsky I, 2018. Imbalance between firing homeostasis and synaptic plasticity drives early-phase Alzheimer's disease. Nat. Neurosci. 21, 463–473. 10.1038/s41593-018-0080-x. [PubMed: 29403035]

Sun M, Bell W, LaClair KD, Ling JP, Han H, Kageyama Y, Pletnikova O, Troncoso JC, Wong PC, Chen LL, 2017. Cryptic exon incorporation occurs in Alzheimer's brain lacking TDP-43 inclusion but exhibiting nuclear clearance of TDP-43. Acta Neuropathol. 133, 923–931. 10.1007/s00401-017-1701-2. [PubMed: 28332094]

Thapa R, Liang B, Liu R, Li Y, 2021. Stereotaxic viral injection and gradient-index lens implantation for deep brain in vivo calcium imaging. J. Vis. Exp. (176), e63049 10.3791/63049.

Tollervey JR, Curk T, Rogelj B, Briese M, Cereda M, Kayikci M, Konig J, Hortobagyi T, Nishimura AL, Zupunski V, et al. , 2011. Characterizing the RNA targets and position-dependent splicing regulation by TDP-43. Nat. Neurosci. 14, 452–458. 10.1038/nn.2778. [PubMed: 21358640]

Vanden Broeck L, Naval-Sanchez M, Adachi Y, Diaper D, Dourlen P, Chapuis J, Kleinberger G, Gistelinck M, Van Broeckhoven C, Lambert JC, et al. , 2013. TDP-43 loss-of-function causes neuronal loss due to defective steroid receptor-mediated gene program switching in Drosophila. Cell Rep. 3, 160–172. 10.1016/j.celrep.2012.12.014. [PubMed: 23333275]

Vanden Broeck L, Callaerts P, Dermaut B, 2014. TDP-43-mediated neurodegeneration: towards a loss-of-function hypothesis? Trends Mol. Med. 20, 66–71. 10.1016/j.molmed.2013.11.003. [PubMed: 24355761]

Vatsavayai SC, Yoon SJ, Gardner RC, Gendron TF, Vargas JN, Trujillo A, Pribadi M, Phillips JJ, Gaus SE, Hixson JD, et al. , 2016. Timing and significance of pathological features in C9orf72 expansion-associated frontotemporal dementia. Brain 139, 3202–3216. 10.1093/brain/aww250. [PubMed: 27797809]

Vucic S, Kiernan MC, 2013. Utility of transcranial magnetic stimulation in delineating amyotrophic lateral sclerosis pathophysiology. Handb. Clin. Neurol. 116, 561–575. 10.1016/B978-0-444-53497-2.00045-0. [PubMed: 24112924]

Wainger BJ, Kiskinis E, Mellin C, Wiskow O, Han SS, Sandoe J, Perez NP, Williams LA, Lee S, Boulting G, et al. , 2014. Intrinsic membrane hyperexcitability of amyotrophic lateral sclerosis patient-derived motor neurons. Cell Rep. 7, 1–11. 10.1016/j.celrep.2014.03.019. [PubMed: 24703839]

Wegorzewska I, Bell S, Cairns NJ, Miller TM, Baloh RH, 2009. TDP-43 mutant transgenic mice develop features of ALS and frontotemporal lobar degeneration. Proc. Natl. Acad. Sci. USA 106, 18809–18814. 10.1073/pnas.0908767106. [PubMed: 19833869]

Williams KL, Fifita JA, Vucic S, Durnall JC, Kiernan MC, Blair IP, Nicholson GA, 2013. Pathophysiological insights into ALS with C9ORF72 expansions. J. Neurol. Neurosurg. Psychiatry 84, 931–935. 10.1136/jnnp-2012-304529. [PubMed: 23463871]

Wils H, Kleinberger G, Janssens J, Pereson S, Joris G, Cuijt I, Smits V, Ceuterick-de Groote C, Van Broeckhoven C, Kumar-Singh S, 2010. TDP-43 transgenic mice develop spastic paralysis and neuronal inclusions characteristic of ALS and frontotemporal lobar degeneration. Proc. Natl. Acad. Sci. USA 107, 3858–3863. 10.1073/pnas.0912417107. [PubMed: 20133711]

Wu LS, Cheng WC, Hou SC, Yan YT, Jiang ST, Shen CK, 2010. TDP-43, a neuro-pathosignature factor, is essential for early mouse embryogenesis. Genesis 48, 56–62. 10.1002/dvg.20584. [PubMed: 20014337]

Zhang L, Liang B, Barbera G, Hawes S, Zhang Y, Stump K, Baum I, Yang Y, Li Y, Lin DT, 2019. Miniscope GRIN lens system for calcium imaging of neuronal activity from deep brain structures in behaving animals. Curr. Protoc. Neurosci. 86, e56 10.1002/cpns.56. [PubMed: 30315730]

Zhang T, Hwang HY, Hao H, Talbot C Jr., Wang J, 2012. Caenorhabditis elegans RNA-processing protein TDP-1 regulates protein homeostasis and life span. J. Biol. Chem. 287, 8371–8382. 10.1074/jbc.M111.311977. [PubMed: 22232551]

Zhang W, Zhang L, Liang B, Schroeder D, Zhang ZW, Cox GA, Li Y, Lin DT, 2016. Hyperactive somatostatin interneurons contribute to excitotoxicity in neurodegenerative disorders. Nat. Neurosci. 19, 557–559. 10.1038/nn.4257. [PubMed: 26900927]

Zhang Y, Denman AJ, Liang B, Werner CT, Beacher NJ, Chen R, Li Y, Shaham Y, Barbera G, Lin DT, 2021. Detailed mapping of behavior reveals the formation of prelimbic neural ensembles across operant learning. Neuron 110 (4), 674–685. 10.1016/j.neuron.2021.11.022. [PubMed: 34921779]

Zhou P, Resendez SL, Rodriguez-Romaguera J, Jimenez JC, Neufeld SQ, Giovannucci A, Friedrich J, Pnevmatikakis EA, Stuber GD, Hen R, 2018. Efficient and accurate extraction of in vivo calcium signals from microendoscopic video data. eLife 7, e28728. [PubMed: 29469809]

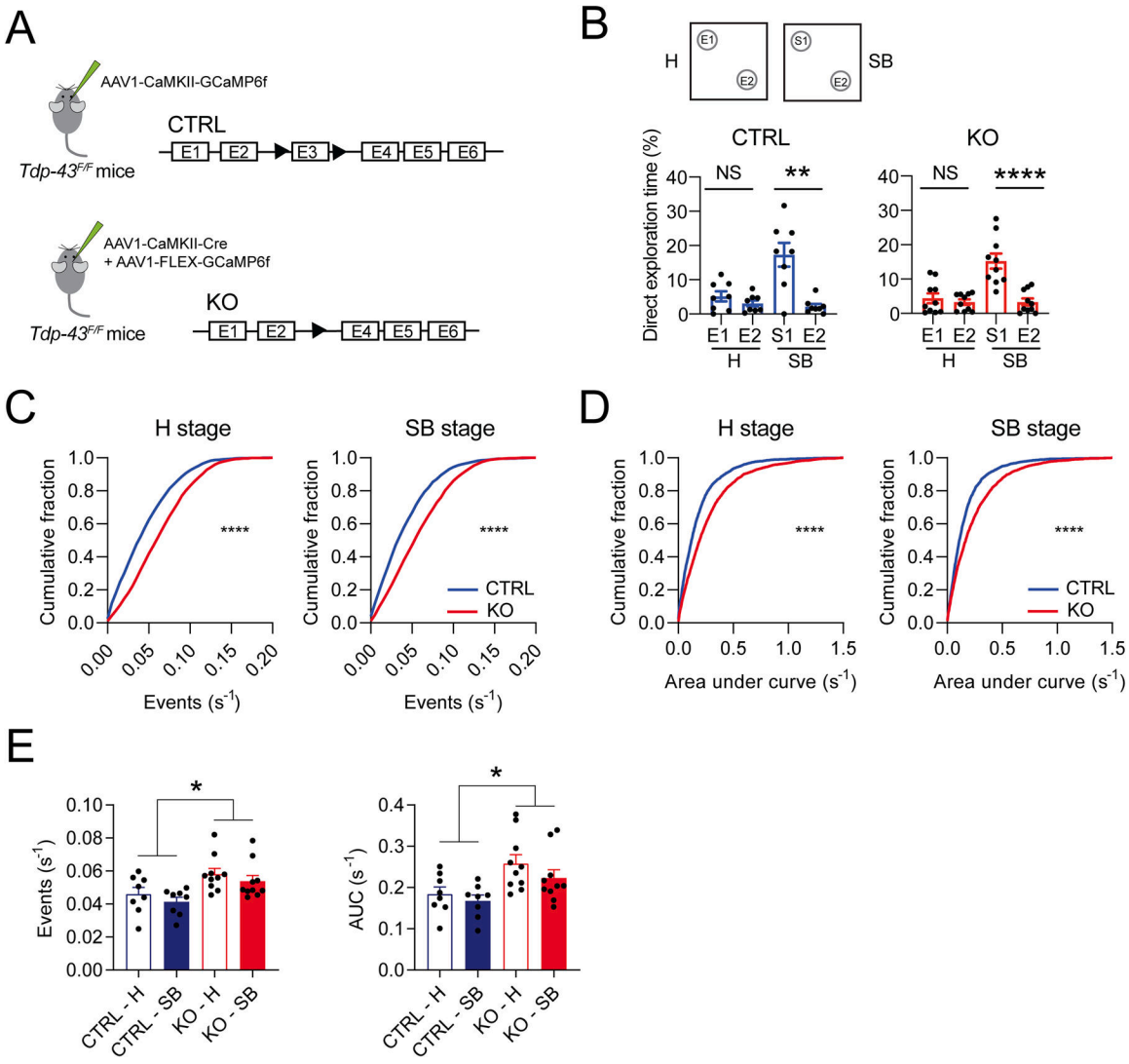

Fig. 1.

Short-term TDP-43 depletion elicits hyperactivity in neuronal calcium activity in the PFC. A. Strategy for generating CTRL and KO mice and labeling excitatory neurons in the PFC of *Tdp-43*$^{F/F}$ mice with a genetically encoded fluorescent calcium indicator, GCaMP6f. CTRL mice were injected with AAV1-CaMKII-GCaMP6f virus to label excitatory neurons with GCaMP6f. KO mice were injected with a viral mix containing AAV1-CaMKII-Cre virus and a Cre-dependent virus, AAV1-CAG-Flex-GCaMP6f, to label TDP-43 depleted excitatory neurons with GCaMP6f. B. Top: schematic paradigm for social behavior test composed of two 10-minutes stages, habituation (H) and sociability (SB) stages. E1 and E2 represent empty containers; S1 represents stranger 1, a never-before-met same sex social target. Bottom: Bar graphs showing the time percentages mice spent during H and SB stages, for direct exploration of E1, E2, and S1, from CTRL (n = 8 mice) and KO (n = 10 mice) groups (Mann-Whitney test). C and D. Cumulative probability distribution panels depicting significant shifts towards higher calcium event frequency (C) and area under curve per second (AUC/s, D) in neuronal calcium traces from KO mice compared to CTRL mice,

during H and SB stages, respectively. CTRL and KO at H stage: n = 2355 and n = 2828 neurons; CTRL and KO at SB stage: n = 2364 and n = 2842 neurons; Kolmogorov-Smirnov test. E. Bar graphs showing comparisons of the averaged calcium event frequency (left panel) and AUC/s (right panel) in neuronal calcium traces from the H and SB stages of individual CTRL and KO mice (CTRL: n = 8 mice; KO: n = 10 mice; Two-way repeated measures ANOVA test). Bar graphs represent mean ± SEM. NS, not significant; *, $p < 0.05$; **, $p < 0.01$; ****, $p < 0.0001$.

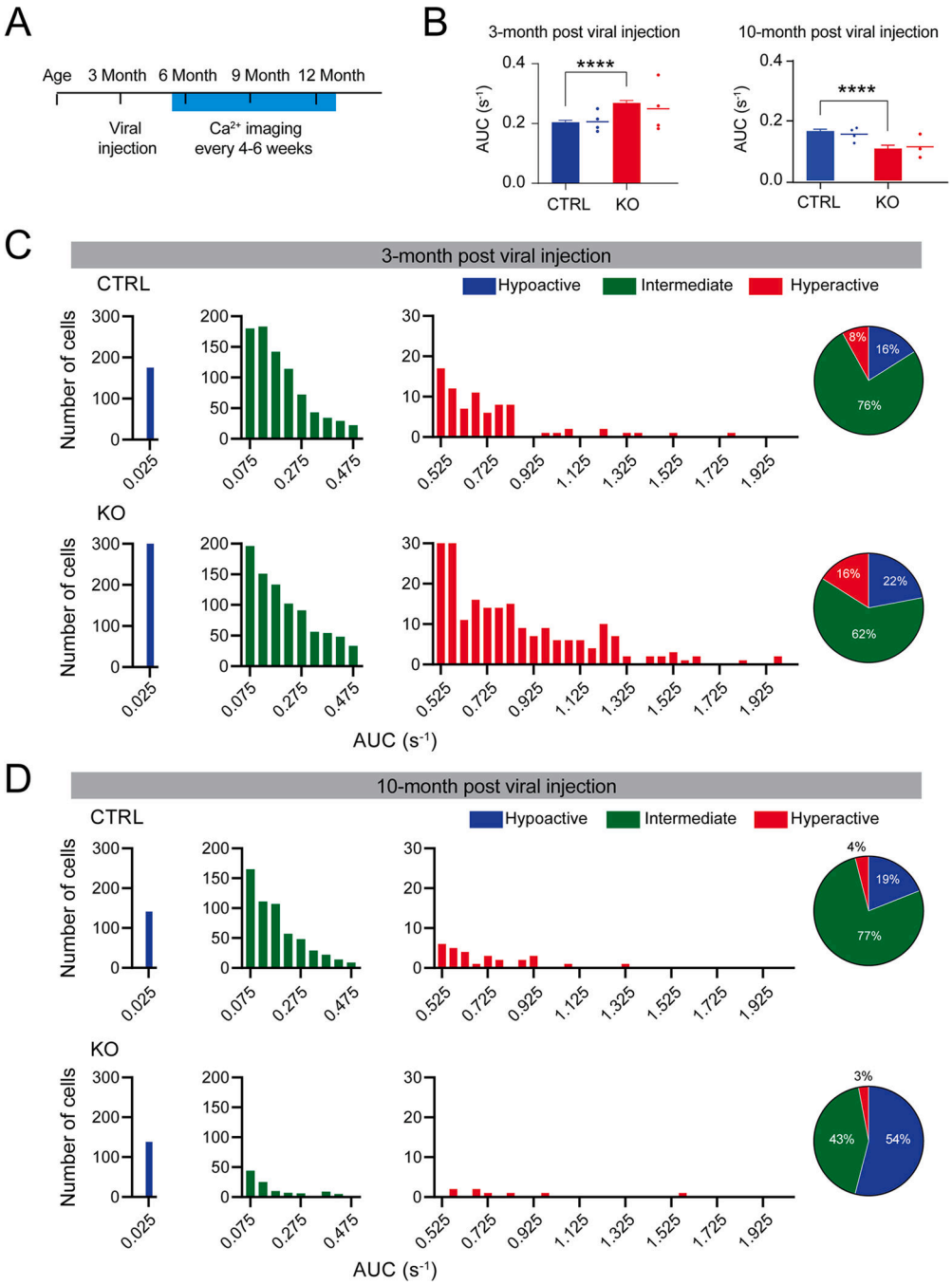

Fig. 2.

Repetitive in vivo calcium imaging reveals dynamic changes in neuronal calcium activity following TDP-43 depletion. A. Schematic diagram showing the experimental timeline. B. Bar graphs represent the averaged area under curve values of neuronal calcium traces during the H stage from CTRL and KO mice. Left panel reveals neuronal hyperactivity in KO mice compared to CTRL mice at 3 months post viral injection (n = 1074 and n = 1400 neurons from 4 CTRL mice and 4 KO mice; Kolmogorov-Smirnov test). Right panel reveals neuronal hypoactivity in KO mice compared to CTRL mice at 10 months post viral injection

(n = 731 and n = 256 neurons from 4 CTRL mice and 4 KO mice; Kolmogorov-Smirnov test). Averaged AUC/s values from individual mice were also indicated besides the bars. C. Histograms illustrating the distribution of area under curve values in calcium traces during the H stage from CTRL group (top, n = 1074 neurons from 4 mice) and KO group (bottom, n = 1400 neurons from 4 mice) at 3 months post viral injection. Pie charts showing the relative proportion of hypoactive, intermediate and hyperactive neurons. D. Histograms illustrating the distribution of area under curve values in calcium traces during the H stage from CTRL group (top, n = 731 neurons from 4 mice) and KO group (bottom, n = 256 neurons from 4 mice) at 10 months post viral injection. Pie charts showing the relative proportion of hypoactive, intermediate and hyperactive neurons. Bar graphs represent mean ± SEM. ****, $p < 0.0001$.

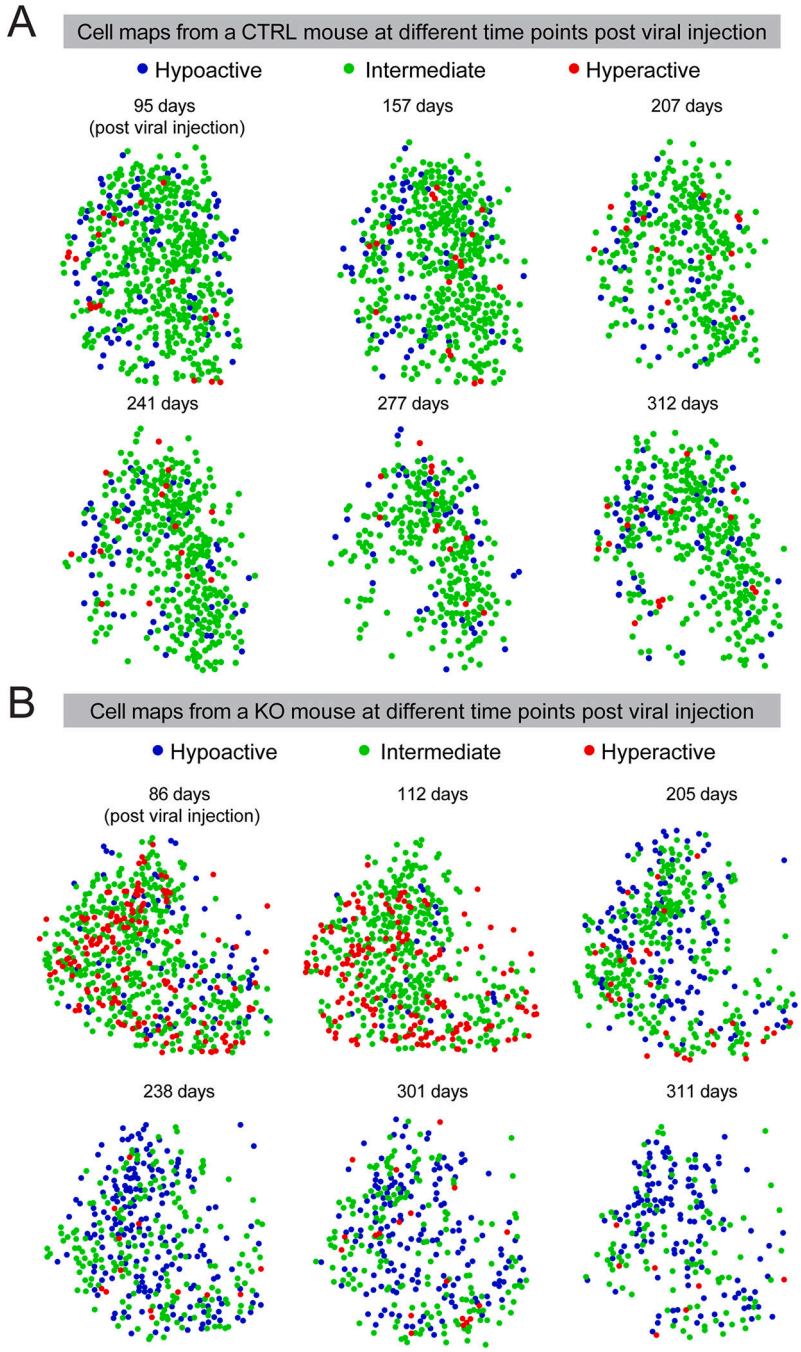

Fig. 3.

Representative cell activity maps across time. Cell activity maps of a representative CTRL mouse (**A**) and KO mouse (**B**) at six different time points as indicated following viral injection. Dots in cell activity maps represent individual neurons. Colors indicate hypoactive (blue), intermediate (green), and hyperactive (red) neurons, according to the area under curve values in calcium traces during the H stage applied with similar thresholds as that of Fig. 2. CTRL cell activity maps display relatively stable proportions of neuronal activity

over time. By contrast, KO cell activity maps reveal large numbers of hyperactive cells at earlier time points while hypoactive cells at later time points.

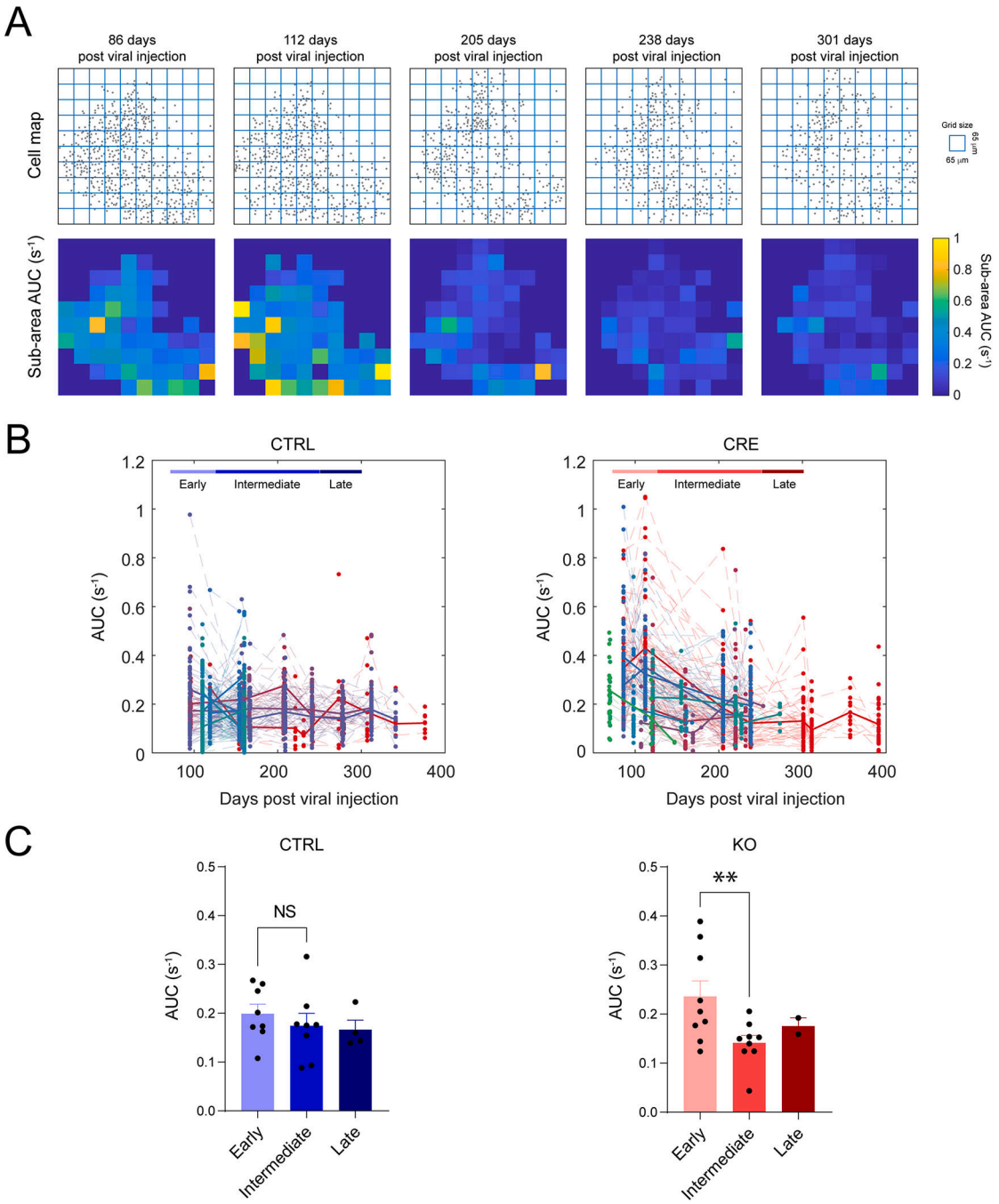

Fig. 4.

Rapid activity declines associated with long term TDP-43 depletion A. Diagrams from a representative KO mouse showing the divided multiple small sub-areas (each with a size of 65 µm by 65 µm, top) and the regional area under curve per second (AUC/s) values averaged from neurons within the same sub-areas at different time points (bottom). B. Plots showing dynamic activity changes over time in regional AUC/s values averaged from neurons within the same divided sub-areas of CTRL and KO mice. Each dot represents AUC/s value from one small sub-area. Dashed lines indicate dynamic activity changes from individual small

sub-areas. AUC/s values were measured only from small sub-areas containing more than 3 active neurons. Solid lines are the averaged AUC/s activity changes from individual mice. Different colors representing different mice. C. Bar graphs are quantifications of the averaged regional AUC/s values measured from individual mice: early (75–125 days post viral injection), intermediate (125–250 days post viral injection), and late (250–300 days post viral injection) stages. CTRL at early, intermediate, and late stages: n = 8, n = 8, and n = 4 mice; KO at early, intermediate, and late stages: n = 9, n = 9, and n = 2 mice. Wilcoxon matched-pairs signed rank test. Bar graphs represent mean ± SEM. NS, not significant; **, $p < 0.01$.

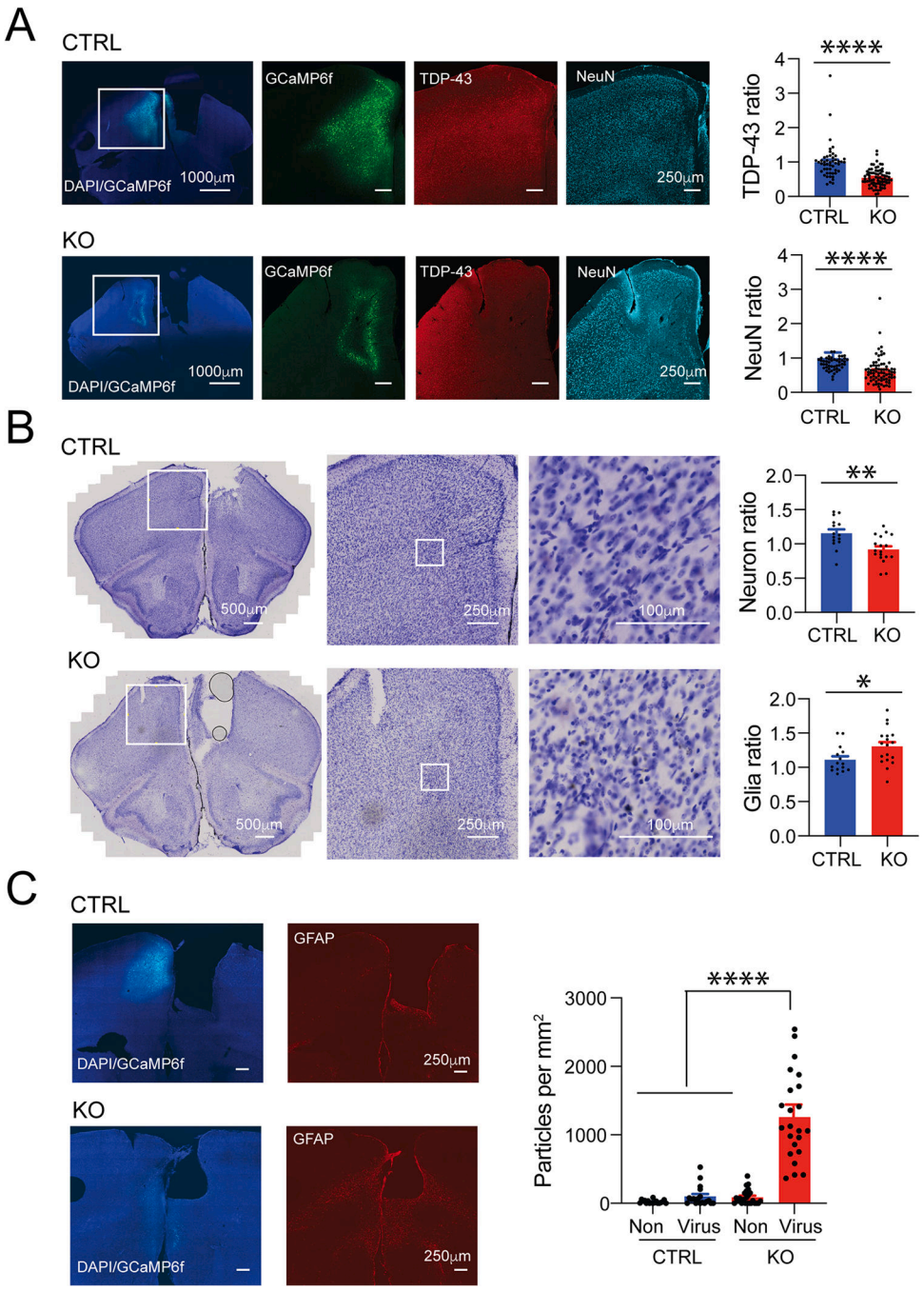

Fig. 5.

Gliosis and neuron loss in TDP-43 deficient areas of the PFC A. Representative immunofluorescence images for TDP-43 and NeuN from a CTRL mouse (top) and a KO mouse (bottom). Images from left to right: DAPI stained whole brain sections (merged green and blue channels, scale bars, 1000 μm); high magnification images of the enclosed area for GCaMP6f (green channel), TDP-43 (red channel), and NeuN (cyan channel). Scale bars, 250 μm. Bar graphs showing quantifications of TDP-43 (top) and NeuN (bottom) from brain sections of CTRL and KO groups. The ratios of positively stained particle

densities between the virus injected and non-injected areas were compared between CTRL and KO groups (CTRL and KO: n = 49 and n = 75 brain sections, Mann-Whitney test). B. Representative Nissl staining images from a CTRL mouse (top) and a KO mouse (bottom). Images from left to right are cresyl violet stained whole brain sections, enlarged PFC regions and high magnification of enclosed areas. Scale bars, 250 μm. Bar graphs showing quantifications of neuronal (top) and glial (bottom) particles in KO mice compared to CTRL mice. The ratios of particle densities between the virus injected and non-injected areas were compared between CTRL and KO groups (CTRL and KO: n = 15 and n = 18 brain sections, Mann-Whitney test). C. Representative immunofluorescence images for GFAP from a CTRL mouse (top) and a KO mouse (bottom). Images showing DAPI stained PFC regions (left, merged green and blue channels) and GFAP immunostaining (right, red channel). Scale bars, 250 μm. Bar graph showing quantification of GFAP positive particle densities of virus injected and non-injected areas from CTRL and KO groups (CTRL and KO: n = 18 and n = 24 brain sections; Kruskal-Wallis test and Dunn's post hoc test). Bar graphs represent mean ± SEM. *, $p < 0.05$; **, $p < 0.01$; ****, $p < 0.0001$.